DFT Analysis of g and ^{13}C Hyperfine Coupling Tensors for Model $Ni^{I}(CO)_nL_m$ ($n = 1-4$, $L = H_2O, OH^-$) Complexes Epitomizing Surface Nickel(I) Carbonyls

Piotr Pietrzyk,[*,†] **Katarzyna Podolska,**[†] **and Zbigniew Sojka**[†,‡]

Faculty of Chemistry and Regional Laboratory for Physicochemical Analyses and Structural Research, Jagiellonian University, Ingardena 3, 30-060 Krakow, Poland

Received: July 30, 2008; Revised Manuscript Received: September 15, 2008

Relativistic calculations within the spin−orbit mean-field (SOMF) approximation, the zero-order regular approximation (ZORA), and the scalar relativistic method based on the Pauli Hamiltonian were performed for the prediction and interpretation of the electronic **g** tensor and ^{13}C hyperfine tensor for a set of model polycarbonyl nickel(I) complexes with aqua or hydroxy coligands. They exhibit extensive similarities with heterogeneous $[Ni^{I}(CO)_n]$−surface complexes produced upon adsorption of carbon monoxide on Ni(I) ions grafted on silica or inside the zeolite channels. Benchmark calculations showing the influence of the exchange-correlation functional on the **g** tensor were carried out for well-defined nickel(I) complexes of known structure. On this basis, the SOMF-B3LYP scheme was chosen for calculations of the **g** tensor, and the obtained results were in satisfactory agreement with literature EPR data found for the $[Ni^{I}(CO)_n]/SiO_2$ system. The calculated **g** and **A**(^{13}C) tensors allowed polycarbonyl complexes of various stereochemistries to be distinguished. The nature of the Δg_{ii} shifts was assessed in terms of the molecular orbital contributions due to the magnetic-field-induced couplings and their structure sensitivity. The noncoincidence of **g** and ^{13}C hyperfine principal axes and their orientation with respect to the molecular framework was also examined. The ability of DFT calculations to follow consistently variations of the EPR parameters induced by stereochemical changes around the Ni(I) center provides an invaluable reference for the interpretation of experimental results.

1. Introduction

Paramagnetic nickel(I) adducts are the key species implicated in various important homo- and heterogeneous catalytic systems including enzymatic and industrial processes.[1,2] For example, nickel-exchanged zeolites play an essential role in the study of the mechanistic aspects of selective catalytic reduction of NO_x[3,4] and olefin dimerization.[5] Homogeneous nickel(I) carbonyls of biologically relevant complexes can mimic the activity of acetylcoenzyme A synthases (acetyl-CoA)[6] or dihydrogen oxidation by hydrogenases.[7] In the latter case, it has been claimed that paramagnetic nickel hydride carbonyl $Ni^{I}(CO)_3H$ represents a good model of the Ni−C bonding situation in key reaction intermediates.[8]

A crucial aspect of the reactivity of carbon monoxide is its coordination to and activation by nickel ions. Surface nickel(I) complexes with increasing numbers of carbonyl ligands can be generated easily by stepwise titration of monovalent nickel with CO adsorbed at various pressures.[9] Analogous formation of diamagnetic $[Ni^{0}(CO)_n]$ complexes with $n = 2-4$ upon interaction of CO with silica-supported highly dispersed nickel particles has also been observed by IR spectroscopy[10] and used for preparative purposes.[11]

To understand the fundamental chemistry of the Ni^{I}−CO unit for controlling the reactivity of this moiety, a molecular-level description of its electronic and magnetic properties in discrete and embedded states is of a great cognitive value. Among many different spectroscopic techniques applied to investigate the $Ni^{I}-(CO)_n$ system, EPR spectroscopy has obviously been widely used because of its paramagnetic nature.[6,9] However, interpretation of the EPR spectral parameters in terms of the molecular structure of the involved surface complexes is not a trivial task, taking into account the intricate nature of the magnetic interactions within the metal−ligand unit and constraints imposed by their usually low symmetry (resulting in noncoincidence of the principal axes of **g** and hyperfine **A** tensors, vide infra).

Thanks to relativistic DFT methods, calculations of EPR parameters are now becoming accessible even for large systems containing transition-metal ions.[12] There are several DFT implementations of **g** tensor calculations, which basically fall into two major classes. The two-component approach, such as the zero-order regular approximation (ZORA),[13] includes spin−orbit coupling treated variationally with the **g** tensor calculated as a first-order property, whereas in the case of one-component methods, such as scalar Pauli[14] or the spin−orbit mean-field (SOMF) approximation,[15] both the magnetic field and the spin−orbit coupling are treated perturbatively, leading to a second-order expression for the **g** tensor.

Calculations of the **g** tensor for nickel(I) complexes have focused so far mostly on biomimetic systems,[8,16,17] homogeneous complexes,[18] and paramagnetic Ni adducts with CO[15] and NO.[19] Because of the limitations of the currently available computational methodologies, it is not easy to construct a very accurate model for detailed analysis of the **g** tensor for complicated large or nonmolecular systems. However, conceptually useful results can be achieved already by analyzing simpler models that can next be embedded into the broad range of conceivable chemical environments with pliant (molecular complexes, enzymes) or rigid (zeolitic framework, amorphous surfaces) ligands.

The present article deals with detailed theoretical electronic and magnetic characterization of model $[Ni^{I}(CO)_nL_m]$ ($n = 1-4$,

---

[*] To whom correspondence should be addressed. E-mail: pietrzyk@chemia.uj.edu.pl. Tel.: +48 12 663 22 24. Fax: +48 12 634 05 15.

[†] Faculty of Chemistry.

[‡] Regional Laboratory for Physicochemical Analyses and Structural Research.

10.1021/jp8067848 CCC: $40.75

$L = H_2O$, OH^-) complexes, that can be regarded as well-defined molecular analogues of surface polycarbonyl adducts of Ni^I ions grafted on silica surface or encaged in zeolites.[9] In view of the variety of surface local environments within which the $[Ni^I(CO)_n]$ unit can reside, we investigated more closely the molecular nature of the calculated **g** and ^{13}C hyperfine tensors in terms of the local symmetry and coordination state of the model polycarbonyl Ni(I) complexes, to provide clear-cut guidelines for their assignment and molecular interpretation. Additionally, by using simple molecular models of strictly defined point symmetry, the EPR characterization of nickel(I) polycarbonyls can be rationalized by detailed insight into the magnetic-field-induced couplings between relevant molecular orbitals that contribute to the experimentally observed **g** tensor anisotropy.[20]

Although the DFT calculations of **g** and ^{13}C tensors were restricted to minimal $[Ni^I(CO)_nL_m]$ models, despite the lack of direct EPR data for such systems, generic categories of the **g** tensor−structure relationships can be delineated and associated with the corresponding magnetophore, i.e., a kernel bearing an overwhelming part of the magnetic properties of the whole complex.[21] However, to maintain the chemical context, the calculated data were compared to available EPR parameters for nickel(I) polycarbonyls supported on silica. Indeed, it is well-documented that the surface functional groups ($\equiv SiO_{surf}^-$, $-OH_{surf}$) of the silica support (often complemented by variable numbers of water molecules) play the role of mere ligands and can be inserted in the spectrochemical series close to aqua ligands.[22] The surface groups are bonded to a grafted transition-metal ion in the same way as the donor atoms of the molecular ligands are bonded to a metal ion and, thus, determine the properties of a surface complex.[23] With the principal relationships between the electronic nature of the **g** and **A** tensors and the stereochemistry of the well-defined molecular complexes thus established as a reference, experimental and theoretical work on more involved intrazeolite adducts of nickel(I) polycarbonyls is currently in progress.

2. Computational Details

Geometry optimization was carried out by means of the ADF[24,25] version 2006.01 program suite at the spin-unrestricted level. The exchange-correlation potential of Becke88[26] and Perdew86[27] along with the scalar relativistic ZORA method was applied during geometry optimization. The all-electron basis set denoted as TZP was used for all atoms. The carbonyl complexes were fully optimized using analytic gradients and the BFGS method, with the SCF electron density convergence criterion of 10^{-6} au. The criterion for the optimal geometry was based on the gradient and displacement norm values and the energy value, with thresholds of 10^{-3}, 3×10^{-3}, and 10^{-5} au, respectively.

Single-point calculations of the **g** tensor involved double group symmetry-adapted functions and spin−orbit coupling (SOC) included self-consistently, to account for relativistic effects within the two-component, spin-unrestricted collinear ZORA method.[18,28] In addition, the one-component method due to Schreckenbach and Ziegler[14] was applied. In this formulation of the **g** tensor, scalar relativistic effects are included in the quasirelativistic framework, employing frozen core orbitals in conjunction with the first-order Pauli Hamiltonian. The gauge dependence was solved by using the GIAO (gauge including atomic orbitals) approach. The **g** tensor was also calculated with the approach of Neese implemented in ORCA[29] software, using the mean-field approximation for SOC, including both the spin-own−orbit and spin-other−orbit interactions in the exchange term.[15] The B3LYP exchange-correlation functional was applied, and the triple-ζ TZV(P) basis set[30] was used for all atoms except for nickel, for which the more accurate CP(PPP)[31] basis set was employed.

The **A** tensor (hyperfine coupling constants) was calculated according to the classical spin-density-based formulation including the SOC contribution as a second-order property, treated at the coupled-perturbed Kohn−Sham level of theory.[32] All hyperfine calculations for ^{13}C nuclei were carried out with the ORCA package using the B3LYP functional. The same basis set as for the **g** tensor calculation was used, except for carbon, for which the EPR-II basis set was found to be more adequate.[33]

3. Results and Discussion

3.1. Benchmark Calculations. For the theoretical treatment of the **g** tensor within the two-component ZORA method, the Zeeman Hamiltonian H^Z (atomic units) expressed in term of the auxiliary function $K = (1 - V/2c^2)^{-1}$ assumes the form $H^Z = (g_e/2c)[(K/2)\boldsymbol{\sigma}\cdot\mathbf{B} + (K/4)\mathbf{B}\cdot\mathbf{L} + \mathbf{B}\cdot\mathbf{L}(K/4) + \boldsymbol{\sigma}\cdot(\nabla K/2 \times \mathbf{A})]$, where $\mathbf{L} = \mathbf{r} \times \mathbf{p}$, $\boldsymbol{\sigma}$ represents the Pauli spin matrices, and c is the velocity of light. The first term represents the electron spin Zeeman, the next two terms are the orbital Zeeman interactions, and the last term is the spin−orbit gauge correction. As mentioned above, within this approach, the relativistic effects are treated variationally.[34] In the alternative one-component method for **g** tensor calculations, scalar relativistic effects are included in the quasirelativistic framework employing frozen core orbitals in conjunction with the first-order Pauli Hamiltonian, $H^{Pauli} = V_{KS} + p^2/2 - p^4/8c^2 + \nabla^2 V_{KS}/8c^2 + {}^1\!/_2\boldsymbol{\sigma}\cdot\mathbf{B} + (1/4c^2)\boldsymbol{\sigma}\cdot(\nabla V_{KS} \times \mathbf{p})$, retaining relativistic mass-velocity ($p^4/8c^2$) and Darwin ($\nabla^2 V_{KS}/8c^2$) operators only.[14,20] In this approach, SOC is treated as a perturbation. The advantage of this approach is that the resultant **g** tensor can be factored into several contributions $g_{ij} - g_e = \Delta g_{ij} = \Delta g_{ij}^{rel} + \Delta g_{ij}^{d} + \Delta g_{ij}^{p}$, where Δg_{ij}^{rel} merges all scalar relativistic corrections whereas the terms Δg_{ij}^{d} and Δg_{ij}^{p} give dia- and paramagnetic contributions, respectively, to $\Delta\mathbf{g}$. In this treatment, the dominant Δg_{ij}^{p} term is dictated mainly by the magnetic-field-induced couplings between occupied and virtual orbitals ($\Delta g_{st}{}^{p,occ-virt}$), accounting in total for about 90% of the $\Delta\mathbf{g}$ shifts in the case of the $[Ni^I(CO)_nL_m]$ complexes.

Within the spin−orbit mean-field (SOMF) approximation, the **g** tensor can be calculated as a second derivative of the energy.[35] At the SCF level, the Δg_{ij} shifts are described by mass-velocity, $\Delta g_{ij}^{mv} = -(\alpha^2/S)\sum_{k,l}P_{kl}^{\alpha\text{-}\beta}\langle\varphi_k|\hat{T}|\varphi_l\rangle$; diamagnetic gauge correction, $\Delta g_{ij}^{d} = 1/(2S)\ \sum_{k,l}P_{kl}^{\alpha\text{-}\beta}\langle\hat{\varphi}_k|\sum_A\xi(\vec{r}_A)[\vec{r}_A\vec{r}_O - \vec{r}_{A,r}\vec{r}_{O,s}]|\varphi_l\rangle$; and a paramagnetic spin−orbit coupling term, $\Delta g_{ij}^{p} = \sum_{k,l}\ \partial P_{kl}^{\alpha\text{-}\beta}/\partial B_i\langle\varphi_k|\hat{h}_j^{SO}|\varphi_l\rangle$, where S represents the total electron spin, α is the fine-structure constant, $P^{\alpha\text{-}\beta}$ represents the spin density matrix, $\zeta(r_A)$ is an approximate radial operator, and h^{SO} is the spatial part of the effective one-electron spin−orbit operator, with $\hat{H}_{SOC} \approx \sum_i\hat{h}_i^{SO}\hat{s}_i$. The derivative of the spin density matrix is calculated from coupled-perturbed Kohn−Sham theory with respect to a magnetic field perturbation (B_i). In this treatment of the **g** tensor, in addition to the one-electron term, a two-electron term is included explicitly. The latter term comprises a Coulomb part treated at the resolution of the identity (RI) approximation; an exchange part involving both spin-own− and spin-other−orbit interactions; and a correlation term that, in practice, contributes negligibly to SOC.

For benchmarking of the computational scheme, we carried out single-point calculations of the **g** tensors within unrestricted ZORA, scalar Pauli, and SOMF approximations for nickel(I)

TABLE 1: Benchmark Calculation of g Tensor Components for Model Nickel(I) Complexes from Various Relativistic DFT Methods

method	g_{xx}	g_{yy}	g_{zz}
	[$L^{Me}NiCO$]		
Pauli-BP	2.108	2.104	2.019
ZORA-BP	2.103	2.099	2.016
SOMF-BP	2.103	2.097	2.018
SOMF-B3LYP	2.174	2.158	2.025
experiment[a]	2.193	2.166	2.014
	[$Ni(L^1)_2$]$^+$		
Pauli-BP	2.260	2.105	2.077
ZORA-BP	2.250	2.097	2.072
SOMF-BP	2.240	2.093	2.072
SOMF-B3LYP	2.348	2.207	2.074
experiment[b]	2.359	2.198	2.070
	[$Ni(L^2)$acetamide]$^+$		
Pauli-BP	2.177	2.114	2.050
ZORA-BP	2.172	2.110	2.047
SOMF-BP	2.164	2.103	2.043
SOMF-B3LYP	2.215	2.136	2.049
experiment[c]	2.287	2.183	2.035

[a] Reference 36. [b] Reference 37. [c] Reference 38.

complexes with known structures, using the experimental EPR parameters as computation targets. For this purpose, the following complexes were selected: (1) a three-coordinate diketimine-nickel(I) complex with a carbonyl ligand ([L^{Me}Ni-CO], L = β-diketiminate ligand),[36] (2) a four-coordinate bis-α-diimine-nickel(I) complex ([$Ni(L^1)_2$]$^+$, L^1 = 2-phenyl-1,4-bis(isopropyl)-1,4-diazabutadiene),[37] and (3) a five-coordinate macrocyclic complex {(R,S,R,S)-[$Ni(L^2)$acetamide]$^+$, L^2 = 1,3,6,8,12,15-hexaazatricyclo[13.3.1.1^{8,12}]}.[38] The obtained results (Table 1) clearly indicate that the method of approximating the spin−orbit interaction has a minor impact on the **g** tensor for all of investigated Ni(I) complexes. Both the ZORA-UN and SOMF schemes gave virtually the same results, slightly better than those due to the Pauli scalar method. The major influence on the calculated **g** tensor is the choice of the exchange-correlation (xc) functional. The calculations using the SOMF-B3LYP scheme were found to be superior to those of SOMF-BP and yielded quantitative agreement with experiment, indicating the importance of inclusion of the exact exchange (HF) in a single-determinant method for **g** tensor calculations.[15] The results obtained for various GGA (generalized gradient approximation) functionals were essentially insensitive to the choice of the individual xc functional. The same trend was observed for the choice of the basis set, unless its quality was lower than triple-ζ, as noted previously.[8,20] Thus, for the computation of the **g** and **A** tensors of the carbonyl complexes, we applied the SOMF-B3LYP scheme, complemented by the scalar Pauli approach for the construction of magnetic coupling diagrams.

3.2. Monocarbonyl [$Ni^I(CO)L_m$] Complexes. The five different monocarbonyl complexes of nickel(I) selected in this study include two tricoordinate [$Ni^ICO(H_2O)_2$]$^+$ species with C_1 and C_s point symmetry, one [$Ni^ICO(H_2O)(OH)$] complex (C_1), and two tetracoordinate [$Ni^ICO(H_2O)_2(OH)$] structures of C_{2v} and C_s symmetry (Figure 1). This allowed us to examine the influence of the number of ligands and their spatial arrangement on the EPR parameters. In the case of the three-coordinate complexes, two generic structures were explored with the so-called T-shape (Figure 1a,b) and Y-shape (Figure 1c) geometries. They were both observed experimentally for nickel(I),[6] although the majority of three-coordinate complexes of transition-metal ions assume a trigonal-planar structure with symmetrically allocated ligands (Y shape) to minimize steric effects.[39]

For all of the calculated monocarbonyls, the CO ligand exhibited nearly linear bonding to the metal center with an internuclear distance of d_{C-O} = 1.160 Å for the structures with an OH^- ligand in the trans position and d_{C-O} = 1.145(6) Å for the structures with a trans aqua ligand or a vacant trans position. The Ni−CO bond length varied between 1.744 and 1.774 Å, whereas the average Ni−OH bond length was equal to 1.971 Å. For weaker H_2O ligands, it was slightly longer ($\langle d_{Ni-OH_2}\rangle$ = 1.985 Å).

All investigated carbonyl structures exhibited a spin doublet ground state, characteristic of the d^9 metal ion configuration. A more in-depth insight into unpaired electron density redistribution was obtained by means of Mulliken population analysis (Table 2). Individual contributions of atomic orbitals (AOs) indicate that, depending on the geometry of the monocarbonyl complex, the $|3d_{z^2}\rangle$ or $|3d_{x^2-y^2}\rangle$ ground state of nickel (both of which were found experimentally[9,17,36]), complemented by a small contribution of L-based orbitals, mainly determine the shape of the spin density repartition (Figure 1). The remaining 3d orbitals do not contribute appreciably to the singly occupied molecular orbital (SOMO) (except for the Y-shape monocarbonyl species, where some admixture of $|3d_{xy}\rangle$ was also observed), despite the fact that, in principle, they can be admixed by symmetry. The change in the ground state is probably most spectacular for the [$Ni^ICO(H_2O)_2$]$^+$ structure, where the $|3d_{z^2}\rangle$ ground state was found in the T-shape geometry (C_1), whereas in the Y-shape geometry (C_s), the $|3d_{x^2-y^2}\rangle$ state is assumed (Figure 1a,c), allowing for straightforward distinction between the two stereochemistries. The characteristic feature of the electronic structure of all investigated monocarbonyl complexes in contrast to polycarbonyl species is a substantial (up to 20%) involvement of the nickel $|4s\rangle$ orbital in the SOMO, which is not expected for d^9 complexes in planar geometry. The spin-density contours (Figure 1) indicate a dominant metal-centered nature of the investigated paramagnets, with the atomic spin population at the nickel site (ρ_{Ni}) varying between 0.85 and 0.93.

The relatively high SOC constant of nickel ($\zeta_{Ni^+} = 565\ cm^{-1}$) gives rise to considerable Δg_{ii} shifts (Table 3), despite the sizable splitting of the energy levels of the monocarbonyl species. The calculated g_{ii} components follow the pattern $g_{xx} > g_{yy} \gg g_{zz} \approx g_e$, in agreement with the dominant $|3d_{z^2}\rangle$ character of the SOMO. For the Y-shape monocarbonyls, the sequence of g_{ii} is reversed in accordance with the dominant $|3d_{x^2-y^2}\rangle$ ground state. The individual g_{ii} values evidently depend on the monocarbonyl geometry. For the tetracoordinate [Ni^ICOL_3] complexes, the **g** tensor exhibits distinctly lower anisotropy in comparison to the tricoordinate [Ni^ICOL_2] structures. Except for the Y-shape species, for all other monocarbonyl complexes, the g_{zz} values vary within a rather narrow range of 2.017−2.034. In the case of tetracoordinate [Ni^ICOL_3] species, the g_{xx} and g_{yy} values are systematically below the values characteristic of [Ni^ICOL_2]. Within the tricoordinate group, the most striking feature is an increase of the g_{xx} and g_{yy} values for the T-shape geometry with respect to the Y-shape geometry of [$Ni^ICO(H_2O)_2$], accompanied by a decrease of the g_{zz} value, which is associated with the change from the $|3d_{x^2-y^2}\rangle$ to the $|3d_{z^2}\rangle$ ground state. As a result, the two conformations can be easily distinguished by the reversed order of the g values with $g_{xx} \approx g_{yy} \gg g_{zz}$ for the T-shape species and $g_{xx} \ll g_{yy} \approx g_{zz}$ for the Y-shape species. Among all investigated monocarbonyls, it was only for the T-shape structures that diagnostic g_{ii} values above 2.3 were

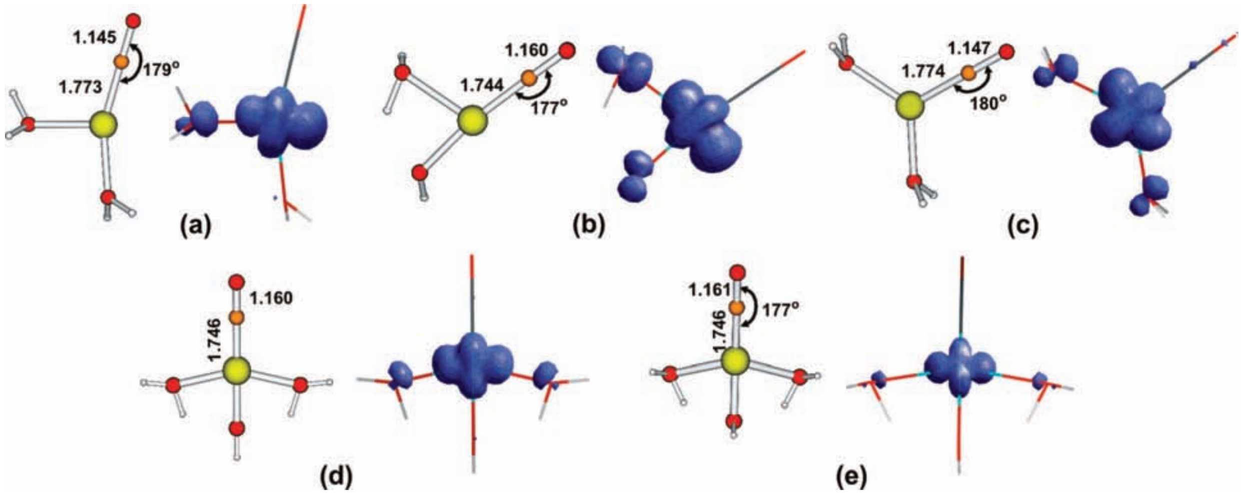

Figure 1. DFT-optimized structures of nickel(I) monocarbonyl complexes: (a) T-shape $[Ni^{I}CO(H_2O)_2]^+$, (b) T-shape $[Ni^{I}CO(H_2O)(OH)]$, (c) Y-shape $[Ni^{I}CO(H_2O)_2]^+$, (d) $[Ni^{I}CO(H_2O)_2(OH)]$, and (e) $[Ni^{I}CO(H_2O)_2(OH)]$. The structures are accompanied by the spin density contour plotted with a 0.007 cutoff. All bond lengths are given in angstroms, and angles are given in degrees.

TABLE 2: Composition of Singly Occupied MO in AO Resolution Derived from DFT Calculations for Various Monocarbonyl $[Ni^{I}COL_n]$ Complexes

	$[Ni^{I}CO(H_2O)_2]^+$	$[Ni^{I}CO(H_2O)(OH)]$	$[Ni^{I}CO(H_2O)_2]^+$	$[Ni^{I}CO(H_2O)_2(OH)]$	
AO contribution	C_1 (T-shape)	C_1 (T-shape)	C_s (Y-shape)	C_{2v}	C_s
ground state	^2A (31a)	^2A (31a)	$^2A'$ (21a')	$^2A_1$ (19a_1)	$^2A'$ (25a')
4s (Ni)	12.0%	18.9%	8.9%	13.9%	10.9%
3p (Ni)	–	1.0%	–	–	–
$3d_{z^2}$ (Ni)	71.7%	37.4%	2.8%	58.2%	25.1%
$3d_{x^2-y^2}$ (Ni)	9.2%	17.3%	74.6%	14.1%	24.6%
$3d_{xy}$ (Ni)	–	–	6.6%	–	–
$3d_{xz}$ (Ni)	–	–	–	–	–
$3d_{yz}$ (Ni)	–	1.9%	–	–	–
2s (C)	2.1%	–	2.8%	3.9%	3.3%
2p (C)	–	–	1.2%	1.2%	–
2s (O)	–	–	–	–	–
2p (O)	–	17.9%	–	1.7%	30.1%

TABLE 3: Calculated g Tensor Components for Various Monocarbonyl $[Ni^{I}COL_n]$ Complexes from SOMF-B3LYP Relativistic DFT Method

structure		**g** tensor		
stoichiometry	symmetry	g_{xx}	g_{yy}	g_{zz}
$[Ni^{I}CO(H_2O)(OH)]$	C_1 (T-shape)	2.326	2.215	2.022
$[Ni^{I}CO(H_2O)_2]^+$	C_1 (T-shape)	2.357	2.249	2.017
	C_s (Y-shape)	2.027	2.239	2.250
$[Ni^{I}CO(H_2O)_2(OH)]$	C_{2v}	2.228	2.195	2.034
	C_s	2.203	2.168	2.030

obtained. These values remain in line with the available experimental data for silica-supported monocarbonyl complex of Ni(I), with $g_{xx} = 2.392$, $g_{yy} = 2.350$, and $g_{zz} = 2.020$,[9] providing a sound argument for the structure assignments. However, the comparison with experimental data has to be carried very carefully. The resolution of the spectra is rather poor, especially regarding the ^{13}C hyperfine structure (vide infra). The data used as references were obtained from the field positions of characteristic points of EPR spectra rather than from computer simulations. This simplified procedure excludes effects of noncoincidence of the **g** and **A** frames, which, in turn, can be taken into account by lowering the spin-Hamiltonian symmetry to monoclinic or even triclinic during computer simulation. Such an approach seems necessary in light of the results showing the relative orientation of the principal axes of the magnetic tensors presented below.

The obtained results can be rationalized in terms of individual MO contributions to the g_{ii} values, according to the partitioning scheme implied by the scalar Pauli Hamiltonian approach. As discussed above, the paramagnetic term ($\Delta g_{ij}^{p,occ-virt}$) largely dominates the total Δg_{ii} shift, so it is reasonable to confine our discussion of the molecular nature of the **g** tensor anisotropy to this overwhelming term.

The principal magnetic couplings to the **g** tensor for the $[Ni^{I}CO(H_2O)(OH)]$ structure in the T-shape configuration calculated with spin-unrestricted resolution are depicted in Figure 2, together with the contours of the magnetically relevant orbitals. Because of the C_1 point symmetry, all possible couplings given by eq 1 are allowed[40]

$$\Delta g_{ij}^{p,occ-virt} \propto \frac{1}{2c(\varepsilon_{virt}^{\sigma} - \varepsilon_{occ}^{\sigma})} \langle \Psi_{virt}^{\sigma} | iL_{x,y,z} | \Psi_{occ}^{\sigma} \rangle \qquad (1)$$

where Ψ_{occ} and Ψ_{virt} are the occupied and the virtual unperturbed Kohn–Sham orbitals, respectively; ϵ is the one-electron energy, L is the orbital momentum operator, and σ stands for α or β spin. To simplify the diagram, only the most important contributions (exceeding 10% of the value of Δg_{iso}) are shown. For the sake of further discussion, the states Ψ_{occ} and Ψ_{virt} can be divided into metal-based and ligand-based spin orbitals.

The g_{xx} component is entirely determined by two strong intrametal β-29a(d_{xz}) ↔ β-31a(d_{z^2}) and β-28a(d_{xy}) ↔ β-31a(d_{z^2}) couplings (Figure 2). Thus, the corresponding matrix element for this contribution is dominated by SOC of the nickel center,

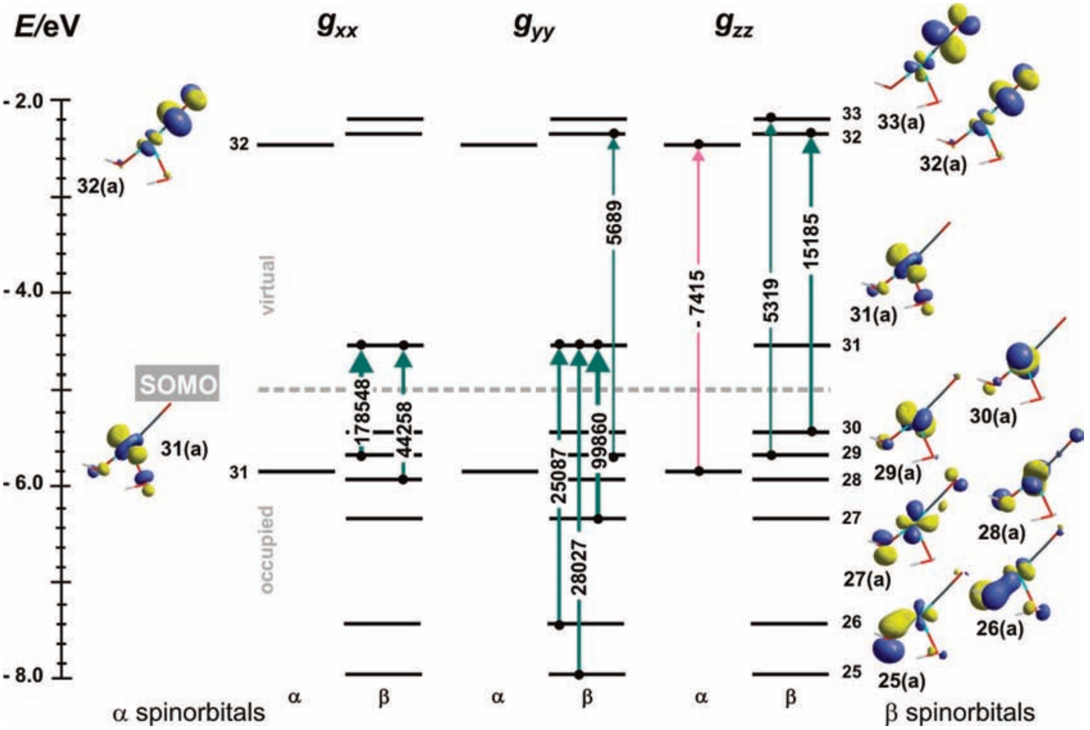

Figure 2. Kohn−Sham orbital diagram for the most important paramagnetic contributions to the **g** tensor components of the T-shape [Ni^{I}CO(H$_2$O)(OH)] complex based on spin-unrestricted BP/TZP scalar relativistic calculations with the Pauli Hamiltonian. The magnetic-field-induced couplings are indicated by arrows, and the corresponding contributions (>10%) are given in parts per million.

which explains the high positive g_{xx} value (Table 2), in agreement with earlier findings for the [L^{Me}NiCO] complex.[26] The contributions to g_{yy} include a dominant intrametal β-27a(d$_{yz}$ − π^*_{OH}) ↔ β-31a(d$_{z^2}$) transition, accompanied by two weaker positive mixed β-25a(σ_{OH} + d$_{xz}$) ↔ β-31a(d$_{z^2}$) and β-26a(π_{OH} + d$_{xy}$) ↔ β-31a(d$_{z^2}$) transitions, along with a metal−ligand β-29a(d$_{xz}$) ↔ β-32a(π^*_{CO} − d$_{xy}$) coupling. The resultant overall Δg_{yy} shift is slightly smaller than the Δg_{xx} shift (Table 2), because it is associated with the transitions between energetically more separated levels. In the case of the g_{zz} component, small positive β contributions [29a(d$_{xz}$) ↔ 33a(π^*_{CO} − d$_{yz}$), 30a(d$_{x^2-y^2}$) ↔ 32a(π^*_{CO} − d$_{xy}$)] and a negative α-31a(d$_{z^2}$) ↔ α-32a(π^*_{CO} − d$_{xy}$) contribution partially cancel, leading to a small deviation of g_{zz} from the g_e value. None of these transitions involve orbitals with large coefficients of the L ligands, indicating that the g_{zz} value is electronically confined to the Ni−CO unit. The g_{xx} value is entirely asociated with the Ni core, whereas only the g_{yy} value is sensitive to the OH ligand. Such a coupling scheme provides a detailed molecular rational for the $g_{xx} > g_{yy} \gg g_{zz}$ sequence that was experimentally observed in the case of the silica-supported monocarbonyl adducts.[9]

The orientation of the **g** tensor principal axes with respect to the molecular framework is shown in Figure 3a. The g_{yy} and g_{zz} axes are located in the O$_{(aq)}$−Ni−C plane, whereas the g_{xx} axis is perpendicular to this plane. The g_{zz} axis is aligned along the lobe of the spin density (Figure 1a,b), forming an angle of 87° with the Ni−C bond, in contrast to the often presumed collinear orientation with the metal−CO bond.[41,42] Because of the perpendicular orientation of the SOMO with respect to the Ni−CO bond, its overlap with the ligand orbitals is poor, giving rise to a very small superhyperfine coupling with the ^{13}C nucleus. The calculated values are equal to A_{xx} = 5 MHz, A_{yy} = 16 MHz, and A_{zz} = 3 MHz and definitely could not be resolved by means of CW-EPR measurements.[9,17]

3.3. Dicarbonyl [Ni^{I}(CO)$_2$(H$_2$O)$_2$]$^+$ complex. The optimized structure of the [Ni^{I}(CO)$_2$(H$_2$O)$_2$]$^+$ complex is shown in Figure 4a. The dicarbonyl exhibits an approximate rectangular planar coordination with the C_{2v} point symmetry. The Ni−CO bond length, d_{Ni-CO} = 1.840 Å, was longer and the internuclear C−O distance, d_{C-O} = 1.143 Å, was slightly shorter than for the monocarbonyl complexes, whereas the distance from nickel to water ligand was found to be equal to 2.101 Å. Both CO ligands are bound almost linearly, forming a Ni−C−O angle of 172° and a C−Ni−C scissor angle of 94°. The resulting spin density contour is depicted in Figure 4a. Population analysis revealed strongly uneven spin density redistribution within the Ni−CO moiety, with 87% placed on Ni and only 5% on CO ligand. According to the atomic composition of the SOMO (Table 4), an A$_2$ ground state, determined by nickel |3d$_{xy}$⟩, exhibits a sizable fraction of carbon-based orbitals (8.2% 2s and 3.3% 2p). Contrary to the monocarbonyl system, the admixture of nickel |4s⟩ orbital to the SOMO is not allowed by symmetry.

The results of the SOMF-B3LYP calculations of the **g** tensor for the [Ni^{I}(CO)$_2$(H$_2$O)$_2$]$^+$ complex are listed in Table 5. They are close to available experimental values reported for [Ni^{I}(CO)$_2$]/SiO$_2$ (g_{xx} = 2.086, g_{yy} = 2.066, g_{zz} = 2.191); unfortunately, they were not ascertained by computer simulation of the EPR spectra.[9]

The magnetic coupling scheme for the dicarbonyl [Ni^{I}(CO)$_2$(H$_2$O)$_2$]$^+$ complex is shown in Figure 5. The g_{xx} component results from β-36b_1(d$_{xz}$) ↔ β-38a_2(d$_{xy}$) intrametal and β-37a_1(d$_{z^2}$) ↔ β-39b_2(π^*_{CO} − d$_{yz}$) mixed metal−ligand couplings, counterbalanced to large extent by a mixed metal−ligand 37a_1(d$_{z^2}$) ↔ 39b_2(π^*_{CO} − d$_{yz}$) transition. The smallest Δg_{yy} shift is determined by intrametal β-35b_2(d$_{yz}$) ↔ β-38a_2(d$_{xy}$) and metal−ligand β-37a_1(d$_{z^2}$) ↔ β-41b_1(π^*_{CO} − d$_{xz}$) transitions, attenuated by α-37a_1(d$_{z^2}$) ↔ α-41b_1(π^*_{CO} − d$_{xz}$), and α-38a_2(d$_{xy}$) ↔ α-39b_2(π^*_{CO} − d$_{yz}$) mixed couplings, which makes this component quite sensitive to the CO ligands. The Δg_{zz} shift is dominated by an intrametal β-34a_1(d$_{x^2-y^2}$) ↔ β-38a_2(d$_{xy}$) coupling, that is only slightly offset by a negative α spin current due to α-34a_1(d$_{x^2-y^2}$) ↔ α-38a_2(d$_{xy}$) and

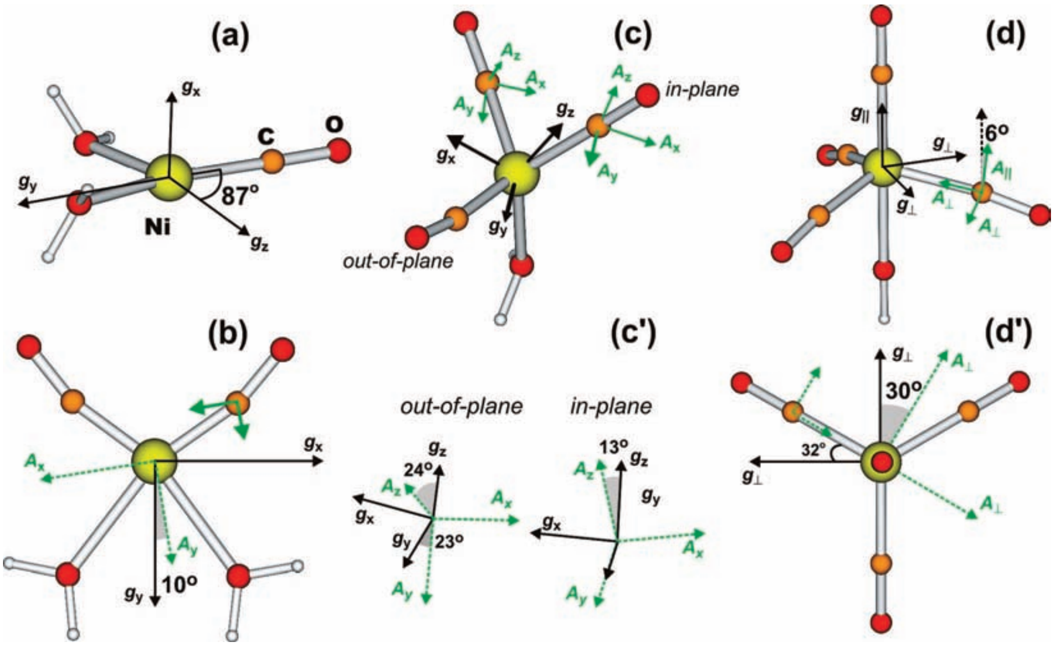

Figure 3. Orientations of the principal directions of the **g** and **A**(^{13}C) tensors with respect to the molecular framework of the carbonyl complexes: (a) T-shape $[Ni^ICO(H_2O)_2]^+$, (b) $[Ni^I(CO)_2(H_2O)_2]^+$, (c,c′) $[Ni^I(CO)_3H_2O]^+$, and (d,d′) $[Ni^I(CO)_4OH]$.

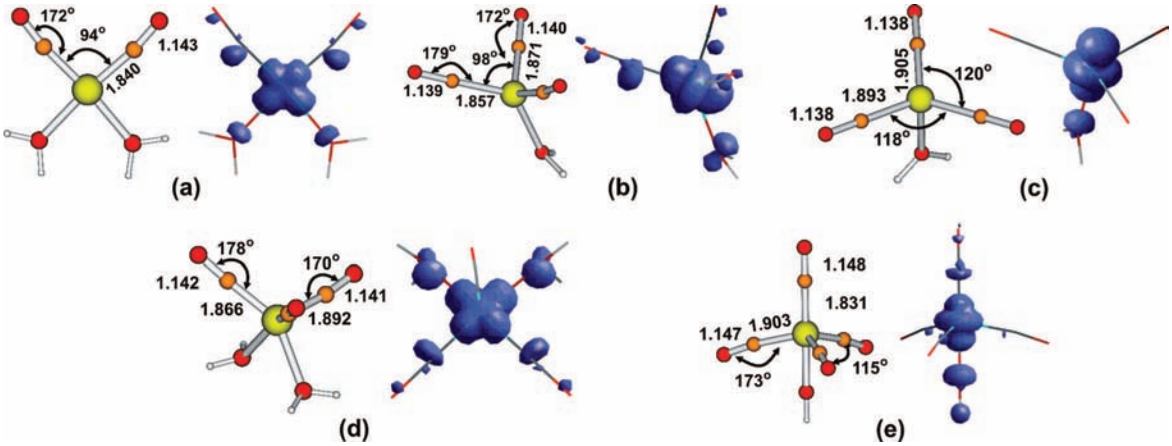

Figure 4. DFT-optimized structures of nickel(I) di-, tri, and tetracarbonyl complexes along with the corresponding spin density contours (0.007 cutoff) for (a) $[Ni^I(CO)_2(H_2O)_2]^+$, (b) $[Ni^I(CO)_3(H_2O)]^+$, (c) planar $[Ni^I(CO)_3(H_2O)]^+$, (d) $[Ni^I(CO)_3(H_2O)_2]^+$, and (e) $[Ni^I(CO)_4(OH)]$. All bond lengths are given in angstroms, and angles are given in degrees.

TABLE 4: Composition of Singly Occupied MO in AO Resolution Derived from DFT Calculations for Di-, Tri-, and Tetracarbonyl $[Ni^I(CO)_nL]$ Complexes

	$[Ni^I(CO)_2(H_2O)_2]^+$	$[Ni^I(CO)_3(H_2O)]^+$		$[Ni^I(CO)_3(H_2O)_2]^+$	$[Ni^I(CO)_4(OH)]$
AO contribution	C_{2v}	C_s	C_s (planar)	C_s	C_{3v}
ground state	$^2A_2$ ($13a_2$)	$^2A'$ ($27a'$)	$^2A'$ ($27a'$)	$^2A''$ ($17a''$)	$^2A_1$ ($20a_1$)
4s (Ni)	–	–	–	–	–
3p (Ni)	3.8%	7.9%	8.7%	3.9%	2.0%
$3d_{z^2}$ (Ni)	–	34.8%	48.4%	–	51.6%
$3d_{x^2-y^2}$ (Ni)	–	–	–	–	–
$3d_{xy}$ (Ni)	–	15.5%	17.1%	–	–
$3d_{xz}$ (Ni)	57.9%	–	–	26.1%	–
$3d_{yz}$ (Ni)	–	–	–	24.5%	–
2s (C)	16.4%	16.7%	9.3%	16.3%	21.4%
2p (C)	6.5%	6.6%	4.4%	6.2%	5.9%
2s (O)	2.4%	–	–	–	3.9%
2p (O)	9.7%	13.6%	6.6%	18.2%	10.4%

α-38a_2(d_{xy}) ↔ α-40a_1($\pi^*_{CO} - d_{x^2-y^2}$) couplings. As a result, the overall Δg_{zz} shift is almost two times larger than that of Δg_{xx} (Table 5), in agreement with the $g_{zz} \gg g_{xx} > g_{yy}$ sequence characteristic of the $|d_{xy}\rangle$ ground state.

The results of relativistic DFT calculations of the **A**(^{13}C) tensor indicate magnetically equivalent character of the two carbonyl ligands. The calculated data (Table 6) remain in a very good agreement with experiment for $[Ni^I(^{13}CO)_2]/SiO_2$ (A_{xx} =

TABLE 5: Calculated g Tensor Components for Di-, Tri-, and Tetracarbonyl [Ni^I(CO)$_n$L] Complexes from SOMF-B3LYP Relativistic DFT Method

structure		g tensor		
stoichiometry	symmetry	g_{xx}	g_{yy}	g_{zz}
$[Ni^I(CO)_2(H_2O)_2]^+$	C_{2v}	2.070	2.047	2.131
$[Ni^I(CO)_3(H_2O)]^+$	C_s	2.131	2.166	2.013
	C_s (planar)	2.308	2.270	2.012
$[Ni^I(CO)_3(H_2O)_2]^+$	C_s	2.089	2.164	2.049
$[Ni^I(CO)_4(OH)]$	C_{3v}	2.109	2.109	2.014

92 MHz, $A_{yy} = 95$ MHz, $A_{zz} = 94$ MHz),[9] indicating that the essential magnetic features of the surface dicarbonyl complex are well captured by its smaller molecular counterpart. Only the calculated A_{zz} component is overestimated by about 10% of its experimental value. Because of the involvement of carbon-based 2s orbitals in the SOMO (Table 4), the ^{13}C superhyperfine interaction is dominated by a large isotropic contact term. After standard decomposition of the calculated $\mathbf{A}(^{13}\mathrm{C})$ tensor [$a_{\mathrm{iso}} = {}^1/_3(A_{xx} + A_{yy} + A_{zz})$, $T_{ii} = A_{ii} - a_{\mathrm{iso}}I$), the resulting isotropic constant was found to be equal to 96 MHz, and the dipolar part ($T_{xx} = -5$ MHz, $T_{yy} = -4$ MHz, and $T_{zz} = 9$ MHz) was quite small.

The coordinate system of the dicarbonyl complex defining the orientation of the principal **g** tensor axes with respect to the molecular framework is shown in Figure 3b. The g_{xx} and g_{yy} axes approximately bisect the O—Ni—C and O—Ni—O angles, respectively, whereas the g_{zz} axis is perpendicular to the $g_{xx}-g_{yy}$ plane, in accordance with the essentially $|d_{xy}\rangle$ ground state. The calculations revealed the noncoincidence of the ^{13}C superhyperfine tensor with respect to the **g** tensor principal axes in the *xy* plane. However, the rotation about the *z* axis is small, not exceeding 10°, and is probably difficult to observe experimentally in powder spectra because of the very small anisotropy of the ^{13}C superhyperfine structure.

3.4. Tricarbonyl $[Ni^I(CO)_3(H_2O)_m]^+$ complexes. The DFT-optimized structures of the investigated tricarbonyl complexes, all of C_s point symmetry, are shown in Figure 4b−d. Two types of tetracoordinate $[Ni^I(CO)_3(H_2O)]^+$ species, a trigonal planar structure (with the sum of the C—Ni—C angles equal to 356°) and a trigonal pyramidal structure (with the sum of the C—Ni—C angles equal to 322°), and a pentacoordinate $[Ni^I(CO)_3(H_2O)_2]^+$ complex were examined to establish the influence of the nickel coordination and the spatial arrangement of CO ligands on EPR parameters.

For all calculated tricarbonyl complexes, two types of CO spatial positions can be distinguished, an in-plane position and an out-of-plane position. The CO ligands exhibited almost linear bonding to the metal center, with the Ni—C—O angle changing between 170° and 180°. The differences in the C—O bond lengths were quite small. For the $[Ni^I(CO)_3(H_2O)]^+$ complex (Figure 4b), the Ni—CO bond lengths were equal to 1.857 Å (for in-plane CO) and 1.871 Å (for out-of-plane CO), which were the shortest values among all tricarbonyl complexes. The softly bonded H$_2$O ligand exhibited a greater bond length of $d_{\mathrm{Ni-OH_2}} = 2.060$ Å in 4-fold coordination, which increased to $d_{\mathrm{Ni-OH_2}} = 2.210$ Å in 5-fold coordination.

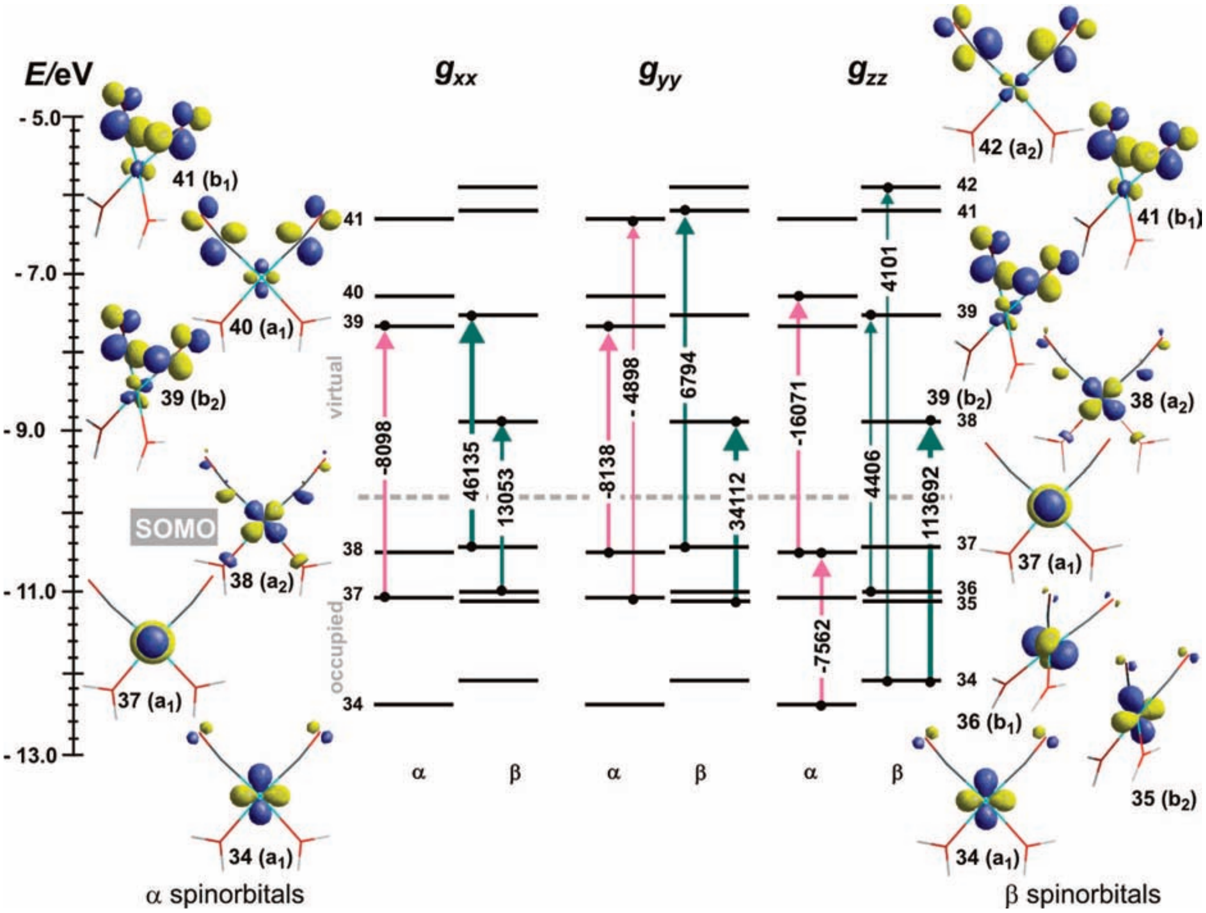

Figure 5. Kohn−Sham orbital diagram for the most important paramagnetic contributions to the **g** tensor components of the $[Ni^I(CO)_2(H_2O)_2]^+$ complex in spin-unrestricted BP/TZP scalar relativistic calculations based on the Pauli Hamiltonian. The magnetic-field-induced couplings are indicated by arrows, and the corresponding contributions (>10%) are given in parts per million.

TABLE 6: Calculated A(^{13}C) Tensor Components for Di-, Tri-, and Tetracarbonyl [Ni^{I}(CO)$_n$L] Complexes from B3LYP-SOMF/EPR-II Relativistic DFT Method

structure			**A** tensor (MHz)		
stoichiometry	symmetry	ligand group	A_{xx}	A_{yy}	A_{zz}
$[Ni^{I}(CO)_2(H_2O)_2]^+$	C_{2v}	2CO	91	92	106
$[Ni^{I}(CO)_3(H_2O)]^+$	C_s	$1CO_{in\text{-}plane}$	93	97	111
		$2CO_{out\text{-}of\text{-}plane}$	43	45	57
$[Ni^{I}(CO)_4(OH)]$	C_{3v}	$1CO_a$	141	141	152
		$3CO_e$	76	88	77

In the case of the pyramidal $[Ni^{I}(CO)_3(H_2O)]^+$ complex (Figure 4b), the atomic spin populations were found to be $\rho_{Ni} = 0.92$ and $\rho_C = 0.05$ for in-plane CO ligands and $\rho_C = 0.01$ for out-of-plane CO ligands. In the planar $[Ni^{I}(CO)_3(H_2O)]^+$ arrangement (Figure 4c), the atomic spin densities indicate that the carbonyl ligands are essentially magnetically equivalent ($\rho_C = -0.02, -0.019, -0.019$). The negative spin density due to polarization is placed on the carbonyl ligands, but the positive spin density, $\rho_{Ni} = 1.06$, is entirely confined to the metal center. For the $[Ni^{I}(CO)_3(H_2O)_2]^+$ complex, the respective values were equal to $\rho_{Ni} = 0.76$ and $\rho_C = -0.01$ for the in-plane CO ligand and $\rho_C = 0.08$ for the out-of-plane CO ligand.

The spin density distribution clearly differentiates between 4-fold (Figure 4b,c) and 5-fold (Figure 4d) structures. In the case of $[Ni^{I}(CO)_3(H_2O)]^+$, the spin density contour is associated essentially with the $|3d_{z^2}\rangle$ ground state, whereas for the $[Ni^{I}(CO)_3(H_2O)_2]^+$ complex, it can be traced to the $|3d_{xy}\rangle + |3d_{yz}\rangle$ hybrid. More detailed insight into the atomic composition of the SOMO is given in Table 4. For the $[Ni^{I}(CO)_3(H_2O)]^+$ complex, the dominant contributions come from the $|3d_{z^2}\rangle$ ground state (34.8% for the 4-fold structure and 48.4% for the planar 4-fold structure) admixed with $|3d_{xy}\rangle$. A noticeable contribution of carbon-based orbitals, especially for the $[Ni^{I}(CO)_3(H_2O)]^+$ complex, is reflected in the magnitude of the calculated ^{13}C hyperfine splitting values (vide infra). The 5-fold coordination is characterized by increased contribution of the metal $|3d_{xy}\rangle/|3d_{yz}\rangle$ hybrid to the SOMO, reaching 50.6%.

In the case of nickel tricarbonyls, the calculated parameters can be compared with the experimental data. However, only the $[Ni^{I}(CO)_3H]$ complex of C_{3v} symmetry and axial **g** tensor ($g_\perp = 2.0674$ and $g_\parallel = 2.0042$), trapped in a krypton matrix, was reported in literature.[43] Its $g_\parallel$ principal axis is oriented along the Ni−H bond, whereas the $g_\perp$ axis is situated in the perpendicular *xy* plane of the molecule. For ^{13}C hyperfine splitting, no experimental values are available. Our SOMF-B3LYP/EPR-II calculations revealed that they are indeed too small ($A_{xx} = -0.8$ MHz, $A_{yy} = 13.8$ MHz, $A_{zz} = 1.8$ MHz) to be resolved in CW-EPR. The calculated **g** tensor components ($g_\perp = 2.0760$ and $g_\parallel = 2.0068$) remain in good agreement with the experiment values and are more accurate than the previous results obtained with ZORA.[8] Analysis of the SOMO composition showed that it is primarily determined by a $|3d_{z^2}\rangle$ (23%)/$|3p_z\rangle$ (22%) hybrid of nickel-based orbitals with significant contribution (21.6%) coming from the hydride ligand. The different character of the SOMO for $[Ni^{I}(CO)_3H]$ as compared to the $[Ni^{I}(CO)_3(H_2O)]^+$ or $[Ni^{I}(CO)_3(H_2O)_2]^+$ complexes (Table 4) is reflected in the smaller anisotropy of the **g** tensor (Table 5). The 5-fold species exhibit the ordering $g_{yy} > g_{zz} > g_{xx}$, in agreement with the $|d_{xy}\rangle/|d_{yz}\rangle$ ground state, and the 4-fold $[Ni^{I}(CO)_3(H_2O)]^+$ complex gives rise to the sequence $g_{yy} > g_{xx} \gg g_{zz}$ characteristic of the $|d_{z^2}\rangle$ ground state. The latter resembles more closely the situation found in the case of supported $[Ni^{I}(CO)_3]/SiO_2$ tricarbonyls with g_{xx} (2.162) > g_{yy} (2.200) ≫ g_{zz} (2.005).[9] Thus, we focused our analysis of the **g** tensor on the pyramidal $[Ni^{I}(CO)_3(H_2O)]$ structure, because it can serve as a suitable model of more complicated surface tricarbonyl complexes.

The diagram of magnetic couplings in $[Ni^{I}(CO)_3(H_2O)]^+$ allows for detailed insight into the electronic nature of its **g** tensor (Figure 6). The Δg_{xx} shift is primarily determined by intrametal $\beta\text{-}36a''(d_{xz}) \leftrightarrow \beta\text{-}40a'(d_{z^2})$ coupling augmented by a smaller $\beta\text{-}39a''(d_{xy}) \leftrightarrow \beta\text{-}41a'(\pi^*_{CO} - d_{x^2-y^2})$ contribution slightly attenuated by two negative $\alpha\text{-}39a''(d_{xy}) \leftrightarrow \alpha\text{-}41a'(\pi^*_{CO} - d_{z^2})$ and $\alpha\text{-}36a''(d_{xz}) \leftrightarrow \alpha\text{-}40a'(d_{z^2})$ transitions. In the case of the g_{yy} component, the overriding contributions are due to the $\beta\text{-}37a'(d_{x^2-y^2}d_{z^2}) \leftrightarrow \beta\text{-}40a'(d_{z^2})$ and $\beta\text{-}38a'(d_{x^2-y^2}) \leftrightarrow \beta\text{-}40a'(d_{z^2})$ intrametal terms. The smallest shift observed for the g_{zz} component is associated with the $\beta\text{-}33a'(\sigma_{CO} + d_{z^2}) \leftrightarrow \beta\text{-}42a''(\pi^*_{CO} - d_{xz})$, $\beta\text{-}36a''(d_{xz}) \leftrightarrow \beta\text{-}43a'(\pi^*_{CO} - d_{x^2-y^2})$, $\beta\text{-}39a''(d_{xy}) \leftrightarrow \beta\text{-}43a'(\pi^*_{CO} - d_{x^2-y^2})$, $\alpha\text{-}28a'(\pi_{CO}) \leftrightarrow \alpha\text{-}42a''(\pi^*_{CO} - d_{xz})$, and $\alpha\text{-}40a'(d_{z^2}) \leftrightarrow \alpha\text{-}42a''(\pi^*_{CO} - d_{xz})$ transitions. The positive β and negative α couplings (on the order 4000−6000 ppm), shown in Figure 6, involve mostly mixed metal−ligand orbitals and tend to mutually cancel each other, leading to a small overall shift. It is characteristic that, despite the rather complex nature of the involved couplings, it is possible to distinguish one or two dominating transitions of intrametal (g_{xx} and g_{yy}) and metal−ligand (g_{zz}) character for each g_{ii} component, as the remaining couplings largely suppress each other in α and β spin currents.

The calculated ^{13}C hyperfine tensor reflects the nonequivalent character of the CO ligands in the $[Ni^{I}(CO)_3(H_2O)]$ complex. For the in-plane CO, the hyperfine coupling is twice as large as for the out-of-plane CO (Table 6), in accordance with the spin density contributions between the two types of ligands (Figure 4b). The only available experimental A_{zz} component, equal to 104 MHz for the in-plane and 52 MHz for the out-of-plane ^{13}CO ligands in the $[Ni^{I}(CO)_3]/SiO_2$ system[9] confirms the close stereochemical resemblance with the model $[Ni^{I}(CO)_3(H_2O)]^+$ complex, inferred previously form the analysis of the **g** tensor.

Because of the low C_s point symmetry of the $[Ni^{I}(CO)_3(H_2O)]^+$ complex, for correct description of the EPR spectra, mutual alignment of the principal **g** and ^{13}C tensor axes has to be ascertained. The spatial orientation of the principal axes of the two tensors with respect to molecular axes is shown in Figure 3c,c′. The g_{zz} axis is tilted from the in-plane CO−Ni bond by 16°, whereas the g_{xx} axis bisects the C−Ni−C angle, formed by two equivalent out-of-plane CO ligands. For the in-plane situation, the two tensors share a common *y* axis and are rotated in the *xz* plane (Figure 3c′). For the out-of-plane CO ligands, however, where no common symmetry element can be found, all **A** and **g** principal axes are noncoincident, with g_{yy} and A_{yy} axes deflected by an angle of 24°.

3.5. Tetracarbonyl [Ni^{I}(CO)$_4$OH] complex. The calculated geometry of the tetracarbonyl $[Ni^{I}(CO)_4OH]$ complex is shown in Figure 4e. The structure was optimized within the C_{3v} point symmetry with three slightly bent [∠(Ni−C−O) = 173°] equatorial (CO_e) and one linear apical (CO_a) carbonyl ligands. The hydroxyl group was placed in the trans position with respect to CO_a. The Ni−C bond for apical CO_a ($d_{Ni-CO_a} = 1.831$ Å) is shorter than that of the three equivalent CO_e ligands ($d_{Ni-CO_e} = 1.903$ Å). Figure 4e shows the spin density contour in the $[Ni^{I}(CO)_4OH]$ complex, which exhibits a shape resembling the nickel $|3d_{z^2}\rangle$ orbital with a notable contribution from the two axial ligands. Mulliken analysis of the atomic spin density population gave $\rho_{Ni} = 0.71$ and $\rho_{CO_a} = 0.10$ for CO_a and ρ_{CO_e}

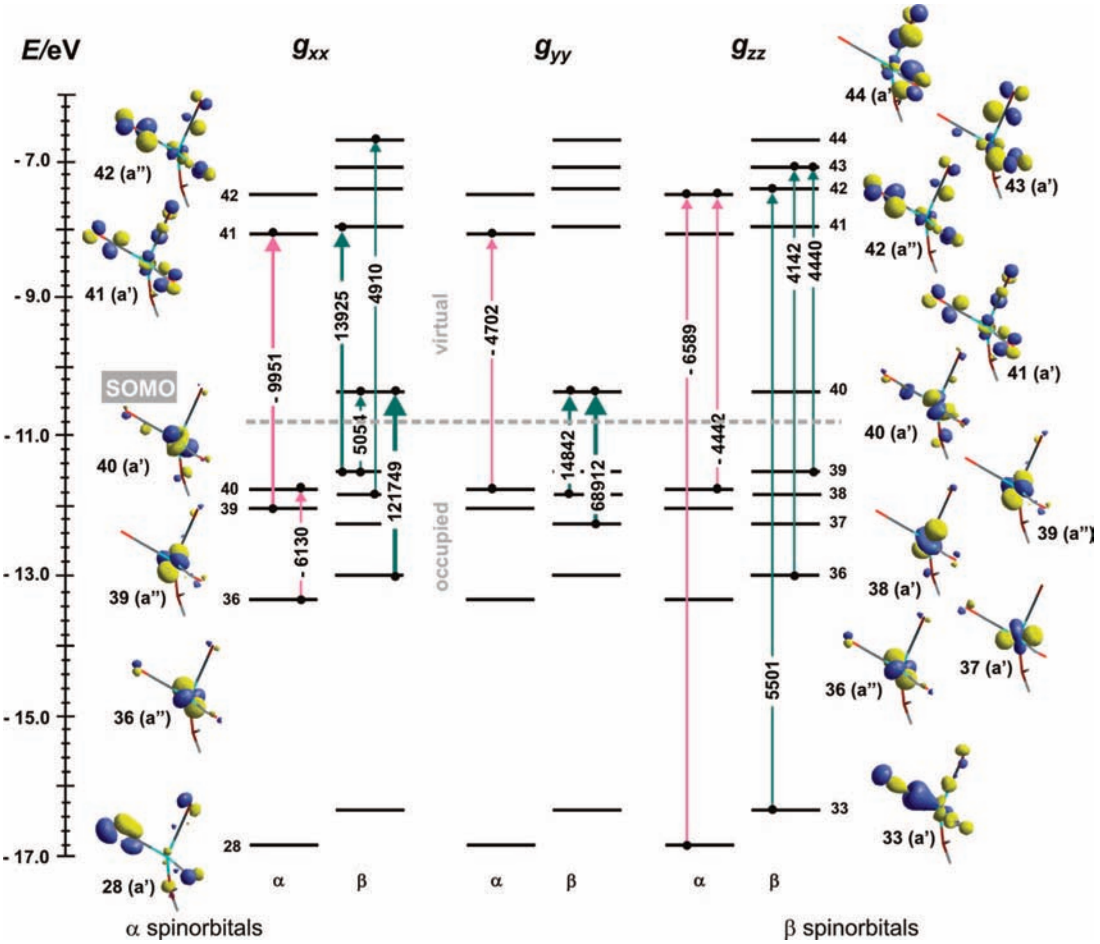

Figure 6. Kohn−Sham orbital diagram for the most important paramagnetic contributions to the **g** tensor components of the $[Ni^{I}(CO)_3(H_2O)]^+$ complex in spin-unrestricted BP/TZP scalar relativistic calculations based on the Pauli Hamiltonian. The magnetic-field-induced couplings are indicated by arrows, and the corresponding contributions (>10%) are given in parts per million.

= 0.04 for CO_e. The associated atomic composition of the $20a_1$ SOMO is given in Table 4, indicating a pronounced metal−ligand nature of the ground state, with 52% contribution from the nickel $|3d_{z^2}\rangle$ orbital and 21% from the carbon $|2s\rangle$ orbital of the CO ligands.

The SOMF-B3LYP calculation of the **g** tensor for the $[Ni^{I}(CO)_4OH]$ complex (Table 5) showed that the perpendicular component ($g_\perp = g_{xx} = g_{yy}$) is smaller (by −0.021) than the experimental value for the similar $Ni^{I}(CO)_4/SiO_2$ surface species ($g_\perp = 2.130$, $g_\| = 2.009$).[9] For the parallel ($g_\| = g_{zz}$) component with a distinctly smaller shift ($\Delta g_\| = 0.007$), the calculated and experimental results showed a smaller deviation. The overall features of the calculated **g** tensor are, however, in line with the experimental values, relating the $[Ni^{I}(CO)_4OH]$ model structure well to the surface $[Ni^{I}(CO)_4]/SiO_2$ complex.

The assumed C_{3v} symmetry of the tetracarbonyl species confers an axial symmetry on its EPR spectrum. The magnetic-field-induced couplings contributing to the parallel and perpendicular components of the **g** tensor are depicted in Figure 7. The couplings α-41,42$e(d_{xy} + d_{x^2-y^2}) \leftrightarrow$ α-46,47$e(\pi^*_{CO} - d_{xz}/d_{yz})$, β-37$a_1(d_{z^2} + \sigma_{CO}) \leftrightarrow \beta$-53$a_2(\pi^*_{CO})$, β-43,44$e(d_{xy} + d_{x^2-y^2}) \leftrightarrow \beta$-45,46$e(\pi^*_{CO} - d_{xz}/d_{yz})$, and β-45,46$e(\pi^*_{CO} - d_{xz}/d_{yz}) \leftrightarrow \beta$-51,52$e(\pi^*_{CO} - d_{xy} - d_{x^2-y^2})$ contributing to the $\Delta g_\|$ shift are very weak and involve mainly the ligand-based orbitals. In the perpendicular direction, the magnetic couplings are doubly degenerate and of more complex nature. The main contributions to the $\Delta g_\perp$ shift involve β-41,42$e(d_{xz}/d_{yz}) \leftrightarrow \beta$-47$a_1(d_{z^2})$ and β-45,46$e(\pi^*_{OH} - d_{xz}/d_{yz}) \leftrightarrow 47a_1(d_{z^2})$ transitions. The remaining couplings shown in Figure 7 are of opposite sign for α and β spin currents and effectively cancel each other. The $g_\perp$ component of the $[Ni^{I}(CO)_4OH]$ complex is quite sensitive to the chemical environment, as its value originates from the couplings between orbitals directly involving the OH-based orbitals (α-SOMO, β-45,46, and β-47).

Information concerning the spatial arrangement of CO ligands in the $[Ni^{I}(CO)_4OH]$ polyhedron can be recovered from the ^{13}C hyperfine structure (Table 6). The ^{13}C hyperfine constants calculated with the B3LYP-SOMF/EPR-II method compare well with the experimental data ($A_\perp = 154$ MHz, $A_\| = 155$ MHz for the axial $^{13}CO_a$ ligand and $A_\perp = 75$ MHz, $A_\| = 70$ MHz for the equatorial $^{13}CO_e$ ligands) found for the $[Ni^{I}(CO)_4]/SiO_2$ complex.[9] They are sufficiently large to be easily resolved experimentally and clearly distinguish between the one axial and three equivalent equatorial ligands, allowing for straightforward assignment of the tetracarbonyl species. As can be inferred from Table 6, the calculated ^{13}C hyperfine splittings are twice as large for the apical as for the equatorial carbonyls. In agreement with the SOMO (Table 4), the ^{13}C hyperfine couplings are dominated by large isotropic terms ($a_{iso} = 145$ MHz for apical CO_a and $a_{iso} = 80$ MHz for equatorial CO_e). The respective anisotropic dipolar parts ($(^{13}C)\mathbf{A}$/MHz = (−4, −4, 8) and $(^{13}C)\mathbf{A}$/MHz = (−4, 7, −3) are quite small, as in the case of other polycarbonyl species. For apical CO, the principal axes of the ^{13}C hyperfine and **g** tensors are coincident because they share all symmetry elements of the C_{3v} point group. However, because the equatorial ligands share only the symmetry plane Ni−(C−O)$_e$, the A_{xx} and

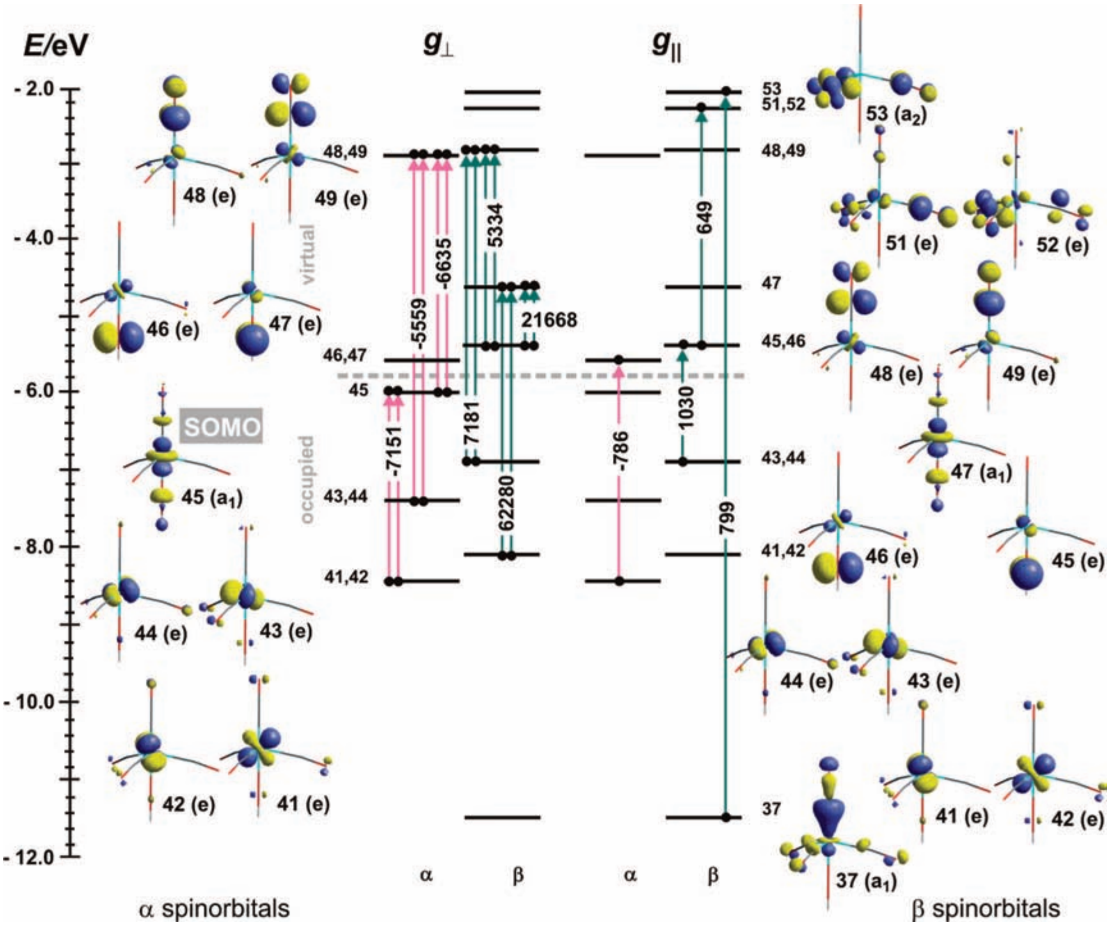

Figure 7. Kohn−Sham orbital diagram for the most important paramagnetic contributions to the **g** tensor components of [Ni^{I}(CO)$_4$(OH)] in spin-unrestricted BP/TZP scalar relativistic calculations based on the Pauli Hamiltonian. The magnetic-field-induced couplings are indicated by arrows, and the corresponding contributions (>10%) are given in parts per million.

$g_\perp$ principal axes are twisted by as much as 30° (Figure 3d′). Moreover, the A_{zz} axis is tilted by 6° with respect to the $g_{\|}$ direction, collinear with the C_3 symmetry axis. The largest A_{yy} splitting is observed along the Ni−C$_e$ bond, where the overlap between the nickel and carbon orbitals is most effective.

3.6. Structural Interpretation of EPR Spectra for Nickel(I) Polycarbonyls. For the structural interpretation of EPR spectra, it is important to understand the qualitative origin of the observed changes in the parameters upon chemical modification of the investigated system. Following previous works on calculation of the **g** and hyperfine tensors for similar transition-metal complexes,[21,44−46] we examined nickel carbonyls [Ni^{I}(CO)$_n$(H$_2$O)$_m$(OH)] with an increasing number of ligands. This allowed for the stepwise exploration of the influence of the coordination environment on the EPR parameters and explicit separation of the geometric and electronic effects.

Changes in the number of CO ligands influence not only the stereochemistry and symmetry of the resultant complexes but also the character of the SOMO and the related anisotropy of the **g** and **A** tensors. These effects can be illustrated with the magnetic-field-induced coupling diagrams shown in Figures 2 and 5−7. In the case of the $|d_{z^2}\rangle$ ground state, such as for the T-shape monocarbonyl species (Figure 2a,b), the g_{zz} component deviates only moderately from the g_e value. For this component, the SOMO and other close-lying occupied states are coupled with states containing a significant admixture of ligand-based π^*_{CO} orbitals; however, because of the high energy gap (3.8 eV), their influence on the **g** tensor shift is rather small. The intrametallic couplings involving dominant nickel d spin orbitals result in appreciable positive shifts observed for g_{xx} and g_{yy} components of the mono- and tricarbonyls.

Direct involvement of L-based orbitals observed, for example, in the case of the [Ni^{I}CO(H$_2$O)(OH)] complex, could be associated with the influence of the support on the EPR spectrum of the analogous surface carbonyl complexes. In the case of monocarbonyl species (Figure 2), it is clear that deep-lying β-25a(π_{OH}) or β-26a(π_{OH} + d$_{xy}$) orbitals of the hydroxy ligand coupled with Ni-based orbitals result in a noticeable shift of the g value (on the order of 10^{-2}), and therefore, only the g_{yy} component bears structural information (a minute $d_{z^2} - \sigma_{H2O}$ contribution to the SOMO is on the order of 10^{-3}). However, the actual nature of the L ligand (H$_2$O or OH$^-$) was shown to be important.[47] For the weakly bound neutral aqua molecules, the ligand-induced contribution to the changes in the **g** tensor values is due to geometrical distortion of the complex stereochemistry. For the more covalently bound hydroxyl ligand, apart from the geometric factor, an electronic effect is also observed {compare the diagrams for [Ni^{I}CO(H$_2$O)(OH)] (Figure 2) and [Ni^{I}CO(H$_2$O)$_2$]$^+$ (Supporting Information, Figure 1S}. Comparison of the results obtained for [Ni^{I}CO(H$_2$O)$_2$]$^+$ and [Ni^{I}CO(H$_2$O)(OH)] (Table 3) shows a distinct decrease of the Δg_{xx} and Δg_{yy} shifts due to the more covalent character of the Ni−OH bond. This can also be seen in the magnetic-field-induced coupling schemes for tetracoordinate structures (Supporting Information, Figures 2S and 3S). Nevertheless, such ligand-induced electronic perturbation of the **g** tensor is too small in magnitude to qualitatively change the character of the resultant spectrum; therefore, essentially similar EPR spectra for oxide surface monocarbonyls can be expected, unless steric effects become important. A similar conclusion is also valid for polycarbonyls. Therefore, the [$Ni^I(CO)_n$] core plays the role of the magnetophore,[21] the spectroscopic properties of which are primarily dictated by the stereochemistry of the CO ligands and only slightly perturbed by the number and spatial arrangement of auxiliary H_2O, OH^-, or $\equiv SiO^-$ ligands.

The observed decrease of **g** tensor anisotropy upon passing from tri- to tetra- and pentacoordinate structures can qualitatively be explained on the basis of the corresponding magnetic coupling diagrams. Taking as an example the T-shape [$Ni^ICO(H_2O)_2$]$^+$ complex and the [$Ni^ICO(H_2O)_2(OH)$] complex (Supporting Information, Figures 1S and 2S), for which the coupling schemes are very similar, one can observe that the absolute values of the individual contributions are systemetically lower for [$Ni^ICO(H_2O)_2(OH)$]. This is related to the enhancement of the respective energy gaps that results in smaller Δg_{ii} shifts. This situation is characteristic of the whole series of mono-, di-, tri-, and tetracarbonyls, where the energy separation between occupied and virtual spin orbitals increased from 0.8 to 1.6 eV. In the case of polycarbonyls, because of extensive mixing of the CO-based orbitals in the majority of the magnetic couplings, the corresponding matrix elements are dominated by the spin−orbit coupling on both the metal center and the ligands. Noting the large difference between SOC values, $\zeta_{Ni^+} = 565$ cm^{-1} and $\zeta_C = 30$ cm^{-1}, the resulting **g** tensor shifts become reduced in magnitude in comparison to those of the monocarbonyl species. For hydroxy complexes, the increased covalency of the Ni—OH bonds and the electronic effect of the OH^- ligand shift the Δg_{ii} values downward, as discussed above.

Comparison of the results revealed that the polycarbonyl complexes can be divided into two classes of different ground states, giving rise to distinct EPR spectra. These two generic classes are schematically shown in Figure 8, along with the SOMO contours. They are accompanied by simulated EPR spectra from the DFT-calculated parameters (assuming typical line widths observed experimentally).[48] The group of the $|3d_{z^2}\rangle$ ground state (e.g., T-shape mono-, tri-, and tetracarbonyls) is characterized by rhombic EPR spectrum with two larger g_{xx}, g_{yy} components, varying between 2.4 and 2.1 (the actual shift depends on the number of CO ligands) and a g_{zz} value close to g_e (Figure 8a). In the case of the $|3d_{x^2-y^2}(d_{xy})\rangle$ ground state (Figure 8b), such as that observed for dicarbonyl complexes, reversed **g** components are expected: one larger (2.2−2.13) and two closer to the g_e value (2.07−2.01). However, a monocarbonyl complex with the $|3d_{x^2-y^2}\rangle$ ground state showing the same type of EPR signal as the one typical for the dicarbonyls has been reported in the literature.[17] Because the ^{13}C hyperfine splitting is not observed in CW-EPR for the monocarbonyl species, regardless of their ground state ($|3d_{z^2}\rangle$ or $|3d_{x^2-y^2}\rangle$), a definitive distinction between the $d_{x^2-y^2}$-type monocarbonyl and dicarbonyl complexes can be achieved by IR spectroscopy, for which one C—O stretching band or two coupled (symmetric and antisymmetric) C—O bands are expected, respectively.

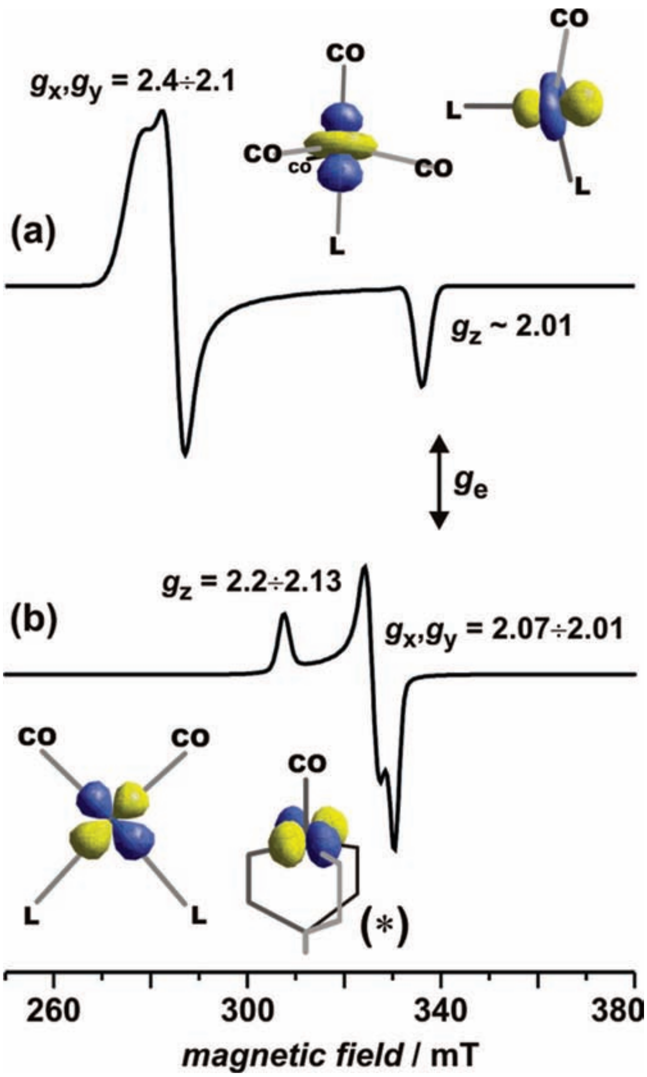

Figure 8. Simulation of X-band ($\nu = 9.5$ GHz) EPR spectra for the generic models of nickel(I) carbonyl complexes characterized by a dominant (a) $|d_{z^2}\rangle$or (b) $|d_{x^2-y^2}\rangle$ ground state. Stick models and SOMO contours are also depicted. (The structure indicated by an asterisk (*) represents the [$PhTt^{tBu}$]—Ni^+CO complex reported in ref 17.)

As shown experimentally,[9,17] the superhyperfine structure due to ^{13}C nuclei can be resolved by means of the conventional CW-EPR technique only for some polycarbonyl complexes (compare Table 6). It can be taken into account by the geometrical relation between the spin density contours (confined essentially to the metal center) and the orientation of the CO ligands. In the cases where the electron overlap allows for direct involvement of the lone pair of CO in the SOMO (dicarbonyl complexes, in-plane CO of tricarbonyl complexes, and axial CO of tetracarbonyl complexes), the calculated hyperfine coupling values are sizable as the hyperfine splitting is dominated by the isotropic interaction. Because of the noncoincidence of the principal axes of the **g** and ^{13}C hyperfine tensors (Figure 3), comparison of the experimental and calculated ^{13}C superhyperfine structure with sizable anisotropy is sensible only in the case of carefully simulated spectra. For tricarbonyl complexes, only the splitting for the in-plane ligand is sufficiently large to be resolved. The experimental data are, however, available only for the A_{zz} component. Possibly this effect is related to extensive **g** and **A** strain, frequently observed in the case of heterogeneous surface complexes leading to broadening of the experimental lines, especially upon passing to higher frequencies.[49] The calculated $A_{xx} = 43$ MHz and $A_{yy} = 45$ MHz splittings for the out-of-plane ligands are too small with respect to typical line widths to be resolved in a continuous-wave experiment.[48]

Despite a few attempts, the ^{13}C splitting has not yet been observed for a monocarbonyl complex. In the case of silica-supported Ni(I) complexes, it was explained by tilting of the CO ligand from the C_3 axis placed along the $3d_{z^2}$ orbital of nickel.[9] Our results show, however, a completely different bonding scheme that eliminates the electronic repulsion between the filled $|3d_{z^2}\rangle$ orbital of Ni and the lone pair of the CO ligand, due to an orthogonal alignment of the Ni—C bond with respect to the main SOMO axis. Similar lack of overlap was observed for the [PhTt^{tBu}]—Ni^{I}CO complex[17] (this situation is shown in Figure 8b), but it is associated with a different character of the SOMO.

4. Conclusions

Molecular model complexes [Ni^{I}(CO)$_n$L$_m$] were used to analyze the electronic nature of the **g** and ^{13}C hyperfine coupling tensors of nickel(I) polycarbonyls at the DFT level. Using benchmark screening, we found that SOMF-B3LYP is the most reliable relativistic scheme for calculation of the magnetic EPR parameters of Ni(I) carbonyls. The results obtained with the SOMF, ZORA, and Pauli methods revealed that the major influence on the **g** tensor calculation is the choice of the exchange-correlation functional. The calculated **g** tensor components for the series of molecular polycarbonyl complexes remain in good agreement with experiment, indicating that the principal features of the Δg shifts observed for the silica-supported polycarbonyls of Ni(I) are well captured by the molecular models. The magnetic coupling diagrams allowed for in-depth molecular interpretation of **g** tensor anisotropy and revealed its structure sensitivity. The lack of ^{13}C superhyperfine structure for the monocarbonyl complexes was explained in terms of the atypical geometrical relation between the spin density contour and the alignment of the CO ligand. In the case of polycarbonyls where ^{13}CO ligand hyperfine splitting was observed, the noncoincidence with the **g** tensor framework was discussed. For all polycarbonyl complexes, two generic types of EPR spectra were distinguished based on their $|3d_{z^2}\rangle$ or $|3d_{x^2-y^2}\rangle$ ground states, and their diagnostic fingerprints were established.

Acknowledgment. Financial support from the Ministry of Science and Higher Education (MNiSW) of Poland, Grant N N204 239334, is acknowledged. The calculations were partially carried out with the computer facilities of CYFRONET-AGH, under Grant no. MEiN/SGI3700/UJ/105/2006. P.P. thanks the Foundation for Polish Science (FNP) for a stipend within the START program.

Supporting Information Available: Figures 1S−3S with additional orbital diagrams showing magnetic-field-induced couplings for [Ni^{I}CO(H$_2$O)$_2$]$^+$ and [Ni^{I}CO(H$_2$O)$_2$(OH)] (C_{2v} and C_s). This material is available free of charge via the Internet at http://pubs.acs.org.

References and Notes

(1) Harrop, T. C.; Mascharak, P. K. *Coord. Chem. Rev.* **2005**, *249*, 3007.

(2) Grochala, W. *Phys. Chem. Chem. Phys.* **2006**, *8*, 1340.

(3) Mosqueda-Jiménez, B. I.; Jentys, A.; Seshan, K.; Lercher, J. A. *J. Catal.* **2003**, *218*, 375.

(4) Dorado, F.; de Lucas, A.; Garcia, P. B.; Romero, A.; Valverde, J. L.; Asencio, I. *Ind. Eng. Chem. Res.* **2005**, *44*, 8988.

(5) Choo, H.; Kevan, L. *J. Phys. Chem. B* **2001**, *105*, 6353.

(6) Eckert, N. A.; Dinescu, A.; Cundari, T. R.; Holland, P. L. *Inorg. Chem.* **2005**, *44*, 7702.

(7) Kubas, G. J. *Chem. Rev.* **2007**, *107*, 4152.

(8) Stein, M.; van Lenthe, E.; Baerends, E. J.; Lubitz, W. *J. Phys. Chem. A* **2001**, *105*, 416.

(9) Bonnevoit, L.; Olivier, D.; Che, M. *J. Mol. Catal.* **1983**, *21*, 415.

(10) Mihaylov, M.; Hadjiivanov, K.; Knözinger, H. *Catal. Lett.* **2001**, *76*, 59.

(11) Hadjiivanov, K.; Mihaylov, M.; Klissurski, D.; Stefanov, P.; Abadjieva, N.; Vassileva, E.; Mintchev, L. *J. Catal.* **1999**, *185*, 314.

(12) Kaupp, M., Bühl, M., Malkin, V. G., Eds. *Calculation of NMR and EPR Parameters. Theory and Applications*;Wiley-VCH: Weinheim, Germany, 2004.

(13) van Lenthe, E.; Baerends, E. J.; Snijders, J. G. *J. Chem. Phys.* **1993**, *99*, 4597.

(14) Schreckenbach, G.; Ziegler, T. *J. Phys. Chem. A* **1997**, *101*, 3388.

(15) Neese, F. *J. Chem. Phys.* **2001**, *115*, 11080.

(16) Stadler, C.; de Lacey, A. L.; Hernandez, B.; Fernandez, V. M.; Conesa, J. C. *Inorg. Chem.* **2002**, *41*, 4417.

(17) Craft, J. L.; Mandimutsira, B. S.; Fujita, K.; Riordan, C. G.; Brunold, T. C. *Inorg. Chem.* **2003**, *42*, 859.

(18) Ray, K.; Weyhermüller, T.; Neese, F.; Wieghardt, K. *Inorg. Chem.* **2005**, *44*, 5345.

(19) Sojka, Z.; Pietrzyk, P.; Martra, G.; Kermarec, M.; Che, M. *Catal. Today* **2006**, *115*, 154.

(20) Patchkovskii, S.; Ziegler, T. *J. Chem. Phys.* **1999**, *111*, 5730.

(21) Pietrzyk, P.; Sojka, Z. *J. Phys. Chem. A* **2005**, *109*, 10571.

(22) Dyrek, K.; Che, M. *Chem. Rev.* **1997**, *97*, 305.

(23) Costa, D.; Martra, G.; Che, M.; Manceron, L.; Kermarec, M. *J. Am. Chem. Soc.* **2002**, *124*, 7210.

(24) te Velde, G.; Bickelhaupt, F. M.; van Gisbergen, S. J. A.; Fonseca Guerra, C.; Baerends, E. J.; Snijders, J. G.; Ziegler, T. *J. Comput. Chem.* **2001**, *22*, 931.

(25) *ADF 2006.01*; Scientific Computing & Modelling NV, Theoretical Chemistry, Vrije Universiteit: Amsterdam, The Netherlands, 2006; available at http://www.scm.com.

(26) Becke, A. D. *J. Chem. Phys.* **1988**, *88*, 2547.

(27) Perdew, J. P.; Wang, Y. *Phys. Rev. B* **1992**, *45*, 13244.

(28) van Wüllen, C. *J. Comput. Chem.* **2002**, *23*, 779.

(29) Neese, F. *ORCA—An ab Initio, Density Functional and Semiempirical Program Package*, version 2.6−00; Lehrstuhl für Theoretische Chemie: Bonn, Germany, 2007.

(30) Schäfer, A.; Huber, C.; Ahlrichs, R. *J. Chem. Phys.* **1994**, *100*, 5829.

(31) Neese, F. *Inorg. Chim. Acta* **2002**, *337C*, 181.

(32) Neese, F. *J. Chem. Phys.* **2003**, *118*, 3939.

(33) Barone, V. In *Recent Advances in Density Functional Methods, Part I*; Chong, D. P., Ed.; World Scientific: Singapore, 1996.

(34) van Lenthe, E.; Wormer, P. E. S.; van der Avoird, A. *J. Chem. Phys.* **1997**, *107*, 2488.

(35) Neese, F. *J. Chem. Phys.* **2005**, *122*, 034107/1−13.

(36) Eckert, N. A.; Dinescu, A.; Cundari, T. R.; Holland, P. L. *Inorg. Chem.* **2005**, *44*, 7702.

(37) Muresan, N.; Chlopek, K.; Weyhermüller, T.; Neese, F.; Wieghardt, K. *Inorg. Chem.* **2007**, *46*, 5327.

(38) Suh, M. P.; Oh, K. Y.; Lee, J. W.; Bae, Y. Y. *J. Am. Chem. Soc.* **1996**, *118*, 777.

(39) Cummins, C. C. *Prog. Inorg. Chem.* **1998**, *47*, 685.

(40) Schreckenbach, G.; Ziegler, T. *J. Phys. Chem.* **1995**, *99*, 606.

(41) Rieger, P. H. *Electron Spin Resonance. Analysis and Interpretation*; Royal Society of Chemistry: Cambridge, U.K., 2007; p 52.

(42) Lionel, T.; Morton, J. R.; Preston, K. F. *J. Chem. Phys.* **1982**, *76*, 234.

(43) Morton, J. R.; Preston, K. F. *J. Chem. Phys.* **1984**, *81*, 5775.

(44) Pietrzyk, P. *J. Phys. Chem. B* **2005**, *109*, 10291.

(45) Freysoldt, C.; Pöppl, A.; Reinhold, J. *J. Phys. Chem. B* **2004**, *108*, 1582.

(46) Pietrzyk, P.; Piskorz, W.; Sojka, Z.; Broclawik, E. *J. Phys. Chem. B* **2003**, *107*, 6105.

(47) Patchkovskii, S.; Ziegler, T. *J. Am. Chem. Soc.* **2000**, *122*, 3506.

(48) Simulation of experimental spectra obtained for the NiBEA system for particular polycarbonyl signals resulted in following line widths (in gauss): $\sigma_x = 35$, $\sigma_y = 25$, $\sigma_z = 17$ for monocarbonyl; $\sigma_x = 18$, $\sigma_y = 25$, $\sigma_z = 22$ for dicarbonyl; $\sigma_x = 26$, $\sigma_y = 21$, $\sigma_z = 10$ for tricarbonyl; and $\sigma_{\|} = 13$, $\sigma_{\perp} = 17$ for tetracarbonyl.

(49) Sojka, Z.; Che, M. *Appl. Magn. Reson.* **2001**, *20*, 433.

JP8067848